



Molecular dynamics studies of CNT-reinforced aluminum composites under uniaxial tensile loading



Bong Kyu Choi ^a, Gil Ho Yoon ^a, Seungjun Lee ^{b,*}

^a School of Mechanical Engineering, Hanyang University, Seoul, Republic of Korea

^b Department of Mechanical, Robotics and Energy Engineering, Dongguk University-Seoul, 100715 Seoul, Republic of Korea

ARTICLE INFO

Article history:

Received 11 March 2015

Received in revised form

6 October 2015

Accepted 26 December 2015

Available online 30 January 2016

Keywords:

A. Metal-matrix composites (MMCs)

B. Mechanical properties

B. Fracture

C. Computational modelling

Molecular dynamics simulation

ABSTRACT

This paper investigates the mechanical behavior of carbon nanotube (CNT)-reinforced aluminum composites (CNT–Al composites) under a tensile loading condition using molecular dynamics (MD) simulations. A review of current computational and experimental studies highlights the benefits of CNT–Al composites from a structural point of view. However, quantitative and qualitative investigations on the improvements due to the inclusion of CNTs are still rare. This study shows that, compared to pure aluminum, the Young's moduli are improved by 31% for (4,4)CNT–Al, 33% for (6,6)CNT–Al, and 39% for (8,8)CNT–Al. Moreover, the corresponding toughness values are significantly enhanced by 37%, 72%, and 100%. Furthermore, the MD simulations provide insights into various fracture behaviors at the atomic scale, including lattice disordering, local changes in lattice structures due to stacking faults, and void nucleation/growth. The component analysis shows that the mechanical properties of CNT–Al composites improve significantly, even with a small amount of CNT, due to the considerable load-bearing capacity of CNT.

© 2016 Elsevier Ltd. All rights reserved.

1. Introduction

After the discovery of carbon nanotubes (CNTs) by Iijima [1], the materials have been extensively studied and utilized in various scientific and engineering applications due to their novel structural and electronic properties. These properties enable remarkable potential applications of CNTs as nano-electronics [2], quantum wire interconnects [3], field emission devices [4,5], composites [6,7], chemical sensors [8], bio-sensors [9], and detectors [10]. Among these applications, CNT-reinforced composites have attracted the attention of researchers in the last few years because of the extraordinary mechanical properties of CNTs [11,12]. As a reinforcing agent, CNTs have superior characteristics of low density (1.3 g/cm³), a high Young's modulus (~1 TPa), high tensile strength (50–150 GPa), and failure strain (~20%). Early studies of CNT-reinforced composites mainly focused on polymer-based composites due to the ease of polymer fabrication [13–17]. However, interest has recently extended to the application of CNTs for metal-matrix composites (MMCs) [7,18–20]. Among the candidates for a metal matrix, aluminum has been popularly considered due to its

richness in the earth's crust, low density, and good mechanical characteristics [21–23].

Most experimental studies on CNT–Al MMCs that have been conducted to date have focused on achieving good dispersion of CNTs within a metal matrix in order to improve the mechanical properties. Tokunago et al. reported that the hardness of a CNT–Al composite was significantly increased and the tensile strength was enhanced to greater than 200 MPa when using high-pressure torsion (HPT) [24]. Bakshi et al. achieved good dispersion of multi-walled carbon nanotubes (MWCNT) in an aluminum matrix using a cold gas spraying process and measured the elastic modulus of the composite to be in the range of 40–229 GPa, via nano-indentation [25]. Kwon et al. reported that the tensile strength of CNT-reinforced aluminum composites was enhanced to three times more than that of pure aluminum with mechanical ball milling due to the uniform dispersion and strong alignment of CNTs [26]. He et al. reported that the mechanical properties of CNT-reinforced aluminum composites fabricated by chemical vapor deposition (CVD) increased with CNT content due to the homogeneous dispersion of CNTs and the strong interfacial bonding between CNTs and metallic matrices [27]. Using an isostatic pressing process, Deng et al. reported that the tensile strength and Young's modulus of CNT–Al composites were enhanced by 35.7% and 41.3%,

* Corresponding author.

E-mail address: sjunlee@dongguk.edu (S. Lee).

respectively, compared to the 2024Al matrix [28]. Esawi et al. revealed that CNT morphology played an important role in the dispersion of MWCNT and affected the mechanical strength of the CNT–Al composite. They showed that the Young's modulus of 2 wt % CNT composites improved by 33% compared to that of pure aluminum [29]. Although previous studies reported the effective role of CNTs in enhancing the mechanical properties of metal composites, the level of relative strengthening ranged widely and quantitative agreement has not yet been reached.

Atomic simulations, such as molecular dynamics (MD) simulations, have been widely used to predict the mechanical properties of nano-scale structures. Particularly for the study of failure mechanisms, MD simulations have significant advantages due to the capability of capturing dynamic atomic behaviors. Despite this advantage, investigations and analyses of the mechanical behaviors of CNT–Al composites using MD simulations are still rare. Using MD simulation, Song et al. investigated the effect of a Ni coating on CNT surfaces with regard to the mechanical strengthening of CNT–Al composites [30]. They showed that the Young's modulus of the CNT–Al composite increased with the density of the Ni coatings, because the Ni coating provided an effective channel for load transfer between the CNT and Al matrix. Xiao et al. studied the effects of vacancy defects of CNTs on the fracture behavior of CNT–Al composites [31]. The study illustrated that even a one-atom vacancy defect dramatically reduced the failure stresses and strains. Recently, Silvestre et al. studied the compressive behavior of CNT–Al composites using MD simulation [32]. They reported that the increase in Young's modulus due to the inclusion of CNT ranged from 50% to 100%, compared to that of pure Al.

As an extension to these studies, we conducted a series of MD simulations to investigate the mechanical behaviors of CNT–Al composites under uniaxial tensile loading. Our simulations shed light on detailed fracture mechanisms, including plastic deformation and crack evolution inside the composite, at the atomic scale. The component analysis reveals the considerable contribution of CNT as a load-bearing material, despite its small volume fraction. In addition, quantitative information on the mechanical properties is provided that shows the effect of CNT diameter. The remainder of this paper is organized as follows. First, in Section 2, the MD model, inter-atomic potentials, and simulation conditions are described. In Section 3, the MD simulation results are provided for the elastic and plastic regions. Finally, in Section 4, our findings are summarized.

2. Computational methods

2.1. Simulation models

The MD simulation model of the CNT–Al composite is shown in Fig. 1. In order to represent the nano-scale structure inside a CNT–Al composite, periodic boundary conditions (PBCs) are applied in the *x*, *y*, and *z* directions. By adopting omnidirectional PBCs, a representative volume inside a composite under a tensile test can be accurately described. The simulations are performed for three different models, shown in Fig. 2. All three models have the same Al matrix geometry with various CNT diameters. The Al matrices are in a square prism shape with the dimensions of 48.3 Å × 48.3 Å × 94.6 Å. The size of the hole in the middle of the aluminum matrix is determined by the CNT diameter. The armchair nanotubes of (4,4)CNT, (6,6)CNT, and (8,8)CNT are placed inside holes of 5.4 Å, 8.1 Å, and 10.8 Å diameter, respectively. Each model contains 15,024 atoms (C: 624 and Al: 14,400), 15,048 atoms (C: 936 and Al: 14,112), and 14,880 atoms (C: 1,248 and Al: 13,632), respectively.

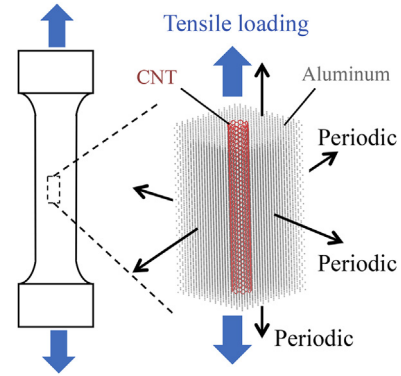


Fig. 1. Schematic of the atomic model for MD simulations, representing the inside of a CNT–Al composite specimen under tensile loading.

2.2. Potentials

Three types of potentials are used to describe the Al, CNT, and Al–CNT interface. For the Al–Al interaction, an Embedded-Atom Method (EAM) potential is employed as follows:

$$E_i = F_\alpha \left(\sum_{j \neq i} \rho_\beta(r_{ij}) \right) + \frac{1}{2} \sum_{j \neq i} \phi_{\alpha\beta}(r_{ij}), \quad (1)$$

where F_α is the embedding energy, which is a function of the atomic electron density ρ_β ; $\phi_{\alpha\beta}$ is a short-range pair potential; and r_{ij} is the distance between atoms *i* and *j*. The two subscripts α and β in $\phi_{\alpha\beta}$ are the element types of atoms *i* and *j*, respectively. The EAM potential developed by Winey et al. [33] is employed because it works very well for metallic Al atoms. The Adaptive Intermolecular Reactive Empirical Bond Order (AIREBO) potential is used for modeling C–C atomic bonds within the CNT [34]. The AIREBO potential is adapted because it has been proven to be accurate to describe the mechanical properties of CNT due to long-range van der Waals and torsional interactions [35]. The total potential is composed of the Reactive Empirical Bond Order (REBO) potential, the Lennard-Jones potential, and the torsional interaction potential as follows:

$$E = \frac{1}{2} \sum_i \sum_{j \neq i} \left[E_{ij}^{\text{REBO}} + E_{ij}^{\text{LJ}} + \sum_{k \neq i} \sum_{l \neq i,j,k} E_{ijkl}^{\text{TORSION}} \right]. \quad (2)$$

The three terms on the right describe the covalent bonding forces, intermolecular interaction, and the dihedral angle effect, respectively. An issue was noted with the original AIREBO potential, the showing of non-physical behaviors at large strain due to improper cutoff functions near a fracture regime. In order to avoid

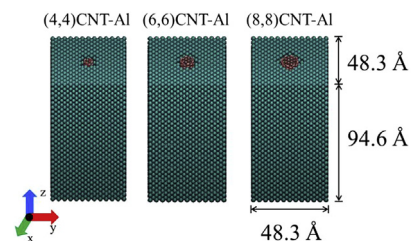


Fig. 2. Three different models with various CNT diameters. The cyan and red atoms denote aluminum and carbon, respectively (For interpretation of the references to color in this figure legend, the reader is referred to the web version of this article.).

this issue, the cutoff parameter of the REBO potential is modified as suggested by Wei et al. [36]. For the interaction between the CNT and Al matrix, van der Waals interactions are considered. To define the C–Al interaction, the Lennard-Jones (LJ) 12-6 potential is adopted as follows:

$$E = 4\epsilon \left[\left(\frac{\sigma}{r} \right)^{12} - \left(\frac{\sigma}{r} \right)^6 \right], \quad (3)$$

where ϵ is the depth of the potential well; σ is the distance where the inter-atomic potential is zero; and r is the distance between two atoms. For the involved LJ parameters of the C–Al interaction, the Lorentz–Berthelot mixing rule is used. The σ and ϵ values are calculated as the arithmetic average of $\sigma_{12} = (\sigma_{11} + \sigma_{22})/2$ and the geometric average of $\epsilon_{12} = \sqrt{\epsilon_{11}\epsilon_{22}}$, respectively. In our study, the values of $\epsilon_{11} = 2.844$ eV and $\sigma_{11} = 3.4$ Å for the carbon atoms [34] and the values of $\epsilon_{22} = 0.4157$ eV and $\sigma_{22} = 2.62$ Å for the aluminum atoms [37] are employed. Thus, the LJ values for the C–Al interactions are calculated as $\epsilon_{12} = 0.03438$ eV, $\sigma_{12} = 3.01$ Å. The cutoff radius is chosen as 10.2 Å, which is larger than $3\sigma_{12} (=9.03$ Å), in order to avoid truncation errors and to fit to the cutoff distance of the AIREBO potential.

2.3. Simulation conditions and mechanical stress

Before conducting the tensile simulations, the three systems are equilibrated over 1 ns with a time step of 1 fs under the NPT ensemble at 300 K and with a pressure of 0 bar to relax the internal stresses. Fig. 3 shows the energy convergence of the three systems.

During the tensile simulations, the simulation box is strained in the z direction at a strain rate of 10^{-6} /ps, which is slower than a typical strain rate used in other MD simulations [38–44]. This is carried out to balance the computation time by considering the issues of undesirable amorphous-disorder deformation with a fast rate, versus calculation expense with a slow rate. The NVT ensemble is applied during the tensile simulation at 300 K. The time step is reduced to 0.5 fs to prevent a blowout of the CNT atoms during fracture.

Mechanical stresses are calculated based on virial stress as follows:

$$\sigma(\mathbf{r}) = \frac{1}{\Omega} \sum_i \left[-m_i \dot{\mathbf{u}}_i \otimes \dot{\mathbf{u}}_i + \frac{1}{2} \sum_{i \neq j} \mathbf{r}_{ij} \otimes \mathbf{f}_{ij} \right], \quad (4)$$

where Ω is the total volume, m_i is the mass of atom i , $\dot{\mathbf{u}}_i$ is the time derivative of \mathbf{u}_i which refers to the displacement vector of atom i relative to a reference position, \otimes is the cross product, \mathbf{r}_{ij} is the distance between the position vectors \mathbf{r}_i and \mathbf{r}_j of atoms i and j , and

\mathbf{f}_{ij} is the interatomic force exerted on atom i by atom j [45]. The total volume Ω is calculated in the equilibrated state. The total volume of the CNT–Al composite is calculated by summing the volume of the aluminum matrix with the hole and the CNT volume. The CNT is assumed to be a cylindrical shell with a thickness of 3.4 Å [46].

3. Results and discussion

Fig. 4 shows the energy variation in the loading process. In Fig. 5, representative snapshots of the MD simulations are presented to show the overall characteristics of the fracture process during the tensile simulation. Fig. 5a shows an equilibrated state before tensile strain is applied to the system. At a strain of 0.1, the CNT moves from the center (Fig. 5b). As the strain increases, a void grows near the top of the aluminum matrix and is accompanied by atomic disorder (Fig. 5c). Next, at a strain of approximately 0.2, the CNT breaks near the void (Fig. 5d), which continues to enlarge and ultimately results in the system separating into two parts (Fig. 5f). A detailed analysis will be discussed in the following sections.

3.1. Elastic regime

Fig. 6 shows the calculated stress (σ)–strain (ϵ) curves. The red, green, blue, and black curves represent the stress–strain curves of (4,4)CNT–Al, (6,6)CNT–Al, (8,8)CNT–Al, and pure aluminum, respectively. In the region of $0 \leq \epsilon \leq 0.07$, the relation between stress and strain is almost linear for all materials. The elastic moduli for the three cases are obtained through regression analysis. The calculated Young's moduli of (4,4)CNT–Al, (6,6)CNT–Al, and (8,8)CNT–Al are 97.01 GPa, 99.02 GPa, and 103.3 GPa, respectively, showing that the Young's moduli increases as the CNT diameter increases. The Young's modulus of pure aluminum is calculated to be 74.24 GPa. Therefore, compared to pure aluminum, the elasticity of the CNT–Al composites of (4,4)CNT–Al, (6,6)CNT–Al, and (8,8)CNT–Al improves by 31%, 33%, and 39%, respectively, due to the CNT. The level of improvement is eventually significant, considering that the amount of CNT is less than 5% of the total volume fraction.

The elasticity of the composites at the macro-scale can be predicted using a simple and well-established mixing rule [32]. The lower bound of the elasticity is calculated as

$$\frac{1}{Y_{\text{CNT-Al}}^{\text{Lower}}} = \frac{V_{\text{CNT}}}{Y_{\text{CNT}}} + \frac{V_{\text{Al}}}{Y_{\text{Al}}}, \quad (5)$$

while the upper bound is obtained using

$$Y_{\text{CNT-Al}}^{\text{Upper}} = V_{\text{CNT}} Y_{\text{CNT}} + V_{\text{Al}} Y_{\text{Al}}, \quad (6)$$

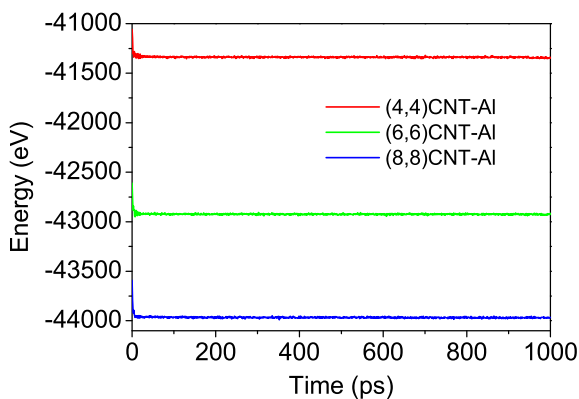


Fig. 3. Total energy variation during relaxation.

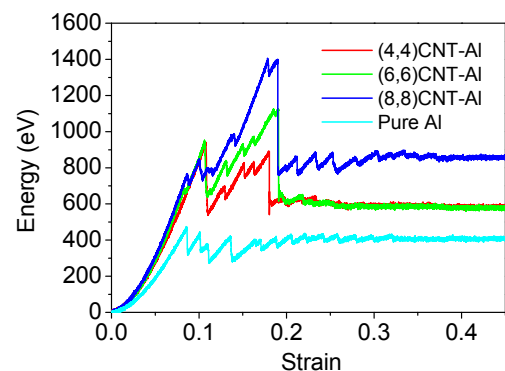


Fig. 4. Total energy variation during the loading process.

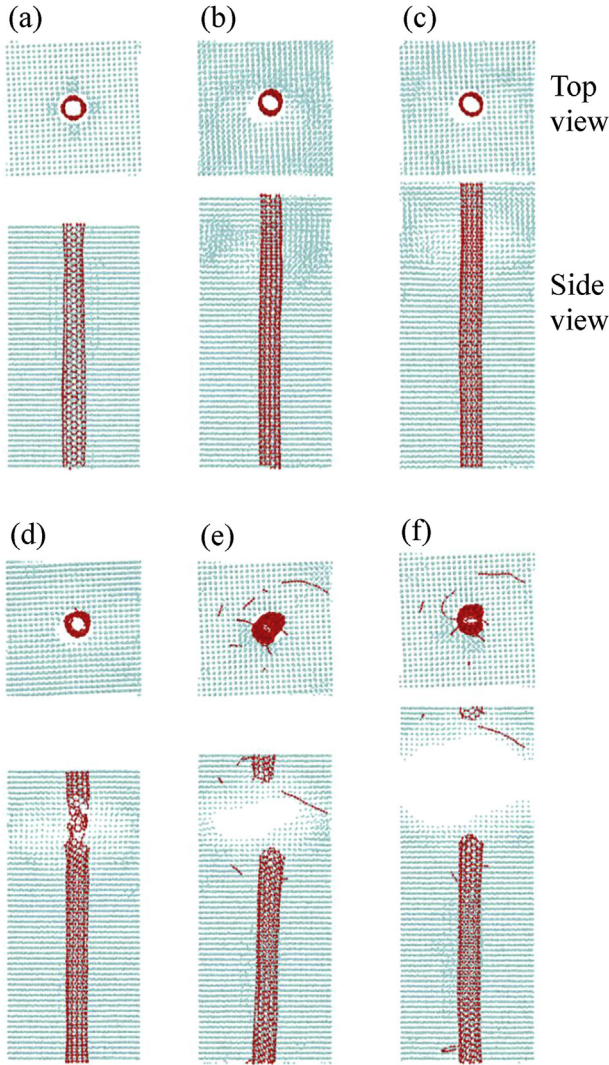


Fig. 5. Snapshots of the MD simulations during the loading process at various strains of (a) 0, (b) 0.11, (c) 0.15, (d) 0.19, (e) 0.25, and (f) 0.45.

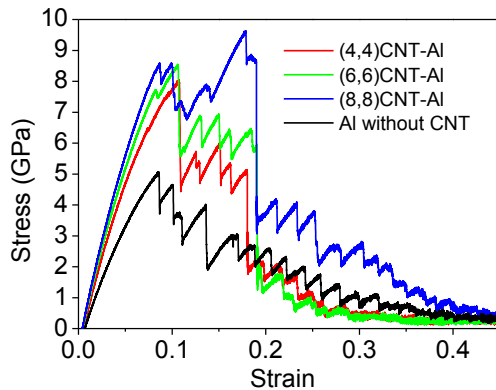


Fig. 6. Stress–strain curves of the three cases of CNT–Al composites with different CNT diameters.

where $\gamma_{\text{CNT-Al}}^{\text{Lower}}$ and $\gamma_{\text{CNT-Al}}^{\text{Upper}}$ are the lower and upper bounds of the composite. The volume fractions of CNT and the Al matrix are denoted by V_{CNT} and V_{Al} . The elastic moduli of the CNT and Al matrix are denoted by Y_{CNT} and Y_{Al} . The elastic moduli are

calculated through a linear fitting of the curves shown in Fig. 7. The calculated lower and upper boundaries of the elastic modulus are summarized in Table 1. The elastic moduli of the three cases lie around the upper bounds because the CNT is aligned parallel to the loading direction, more effectively supporting the loading. This result implies that the linear elasticity theory (i.e., the macro-scale mixing rule) can be applied to the nano-scale. Thus, the framework in this study can be used to predict the elasticity of CNT composites with different metal matrices but similar configurations.

To investigate the contributions of the CNT and Al components to mechanical behaviors, we divide the total stress into the stresses of Al and CNT, and the results are shown in Fig. 7. The CNT stresses vary considerably according to CNT diameter, while the aluminum stresses rarely change. This indicates that the improved stiffness of the composites is mainly due to the effects of the CNTs. In Fig. 7b, the maximum stress of Al decreases as the CNT diameter increases because the size of the hole in the middle of the Al increases. The hole in the middle acts as a defect. Thus the enlarged hole weakens the Al matrix. However, the maximum stress of the CNT–Al composites increases as the CNT diameter increases due to the strong contribution of the CNT inserted into the hole.

In the region of $0.07 \leq \varepsilon \leq 0.1$, the curves show a decrease, particularly the blue and green curves. A magnified view at around 0.08 strain is shown in Fig. 8. The decreases are due to the stress change of the Al matrix, as shown in Fig. 7b. The decrease in the stress curves represents Al atom slippage on the surface of the hole in the middle of the Al matrix. As a result, the hole is slightly enlarged with an asymmetric shape (Fig. 5b). Simultaneously, the CNT that is initially positioned in the middle of the hole moves to

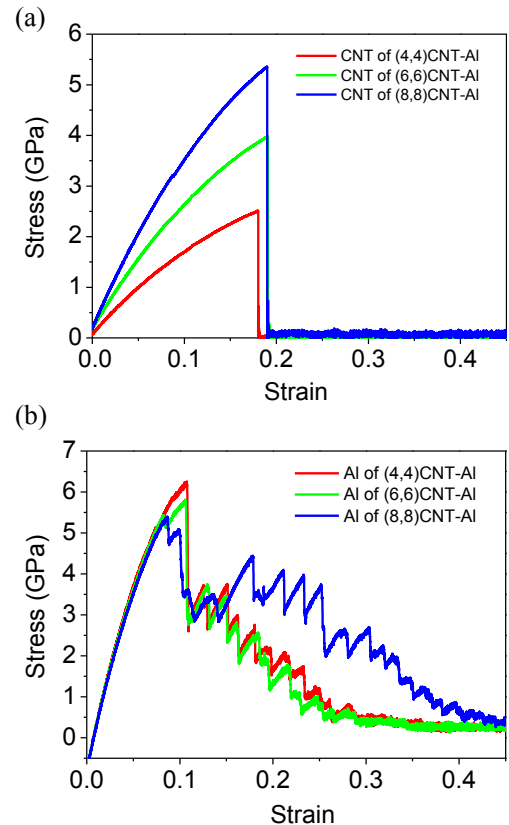
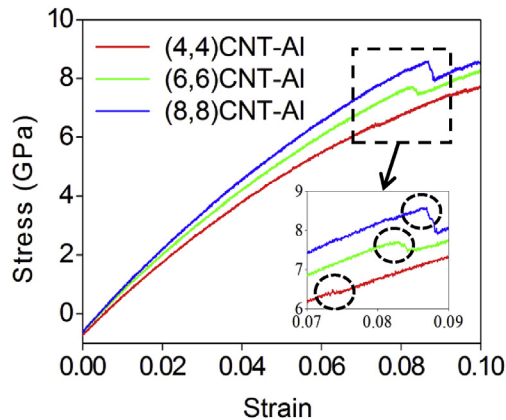


Fig. 7. Stress contribution of each component of (a) CNT and (b) aluminum to the total stress–strain curves in the CNT–Al composite.

Table 1

Volume fractions and elasticity ranges of the CNT–Al composites estimated using the mixing rule.

	Young's modulus (GPa)		Volume fraction (%)		Young's modulus (GPa)	
	CNT γ_{CNT}	Al matrix γ_{Al}	CNT V_{CNT}	Al matrix V_{Al}	Lower bound $\gamma_{\text{CNT-Al}}^{\text{Lower}}$	Upper bound $\gamma_{\text{CNT-Al}}^{\text{Upper}}$
(4,4)CNT–Al	1069.03	74.18	2	98	75.59	94.08
(6,6)CNT–Al	1096.08	74.22	3	97	76.36	104.88
(8,8)CNT–Al	1117.58	74.29	4	96	77.17	116.02

**Fig. 8.** Magnified view of the stress–strain curves in the elastic region, and the magnified curves near the yielding point around 0.08 strain.

the enlarged surface where the atomic slippage occurs. Therefore, the composite accompanies the irreversible atomic movement, which represents a yielding point of typical bulk materials. Similar to the elasticity, the yield stress and yield strain of the composites increase as the CNT diameter increases.

Experimentally, Laha et al. [47] reported that the Young's moduli of CNT-reinforced composites varied from 85 GPa to 120.4 GPa, depending on the composite processing techniques, CNT type, and volume fractions. Another study reported that the Young's modulus was enhanced to 110.2 GPa by using a hot rolling technique [48]. Therefore, the value of approximately 100 GPa obtained in the present study agrees well with the experimentally reported values. Theoretically, a compressive behavior of (6,6)CNT–Al has been reported with two different boundary conditions using MD simulations [32]. In that study, the elastic moduli were calculated as 108 GPa and 142 GPa. Another study was performed to determine the effect of a coating on the CNT surface, and an elastic modulus of 135 GPa was reported for (4,4)CNT–Al without coating [30]. Compared to the other simulation results, the values from our study are rather low. The discrepancy resulted from the application of different boundary conditions: previous studies did not use PBCs, which can minimize the size effect. In the absence of PBCs, the simulation material is surrounded by open space. Thus, the property of the material in the space will strongly depend on the size of the material. In our study, the atomic behaviors of the inner state of a material under a loading condition are described more accurately by using PBCs.

3.2. Plastic regime

After a strain of 0.1, the stress–strain curves decrease largely due to the massive disordering of the aluminum atoms. Fig. 7 shows that the stress curves of CNTs increase continuously, while the aluminum stress curves decrease considerably to around a 0.1 strain. Notably, although most of the mechanical properties, such as elasticity and fracture stress, are enhanced as the diameter of the CNTs increases, the fracture strain shows the opposite trend. This is because as the CNT diameter decreases the hole in the aluminum matrix which serves as a defect is narrower. Thus, the system with a smaller defect fails at a larger strain (Table 2).

The detail fracture behaviors are captured in the MD simulations, and several representative snapshots are presented in Fig. 9. It is observed that the face-centered cubic (FCC) aluminum structure changes to a hexagonal close-packed (HCP) structure due to the stacking fault [40,49], which is captured using common neighbor analysis [50]. Void generation and growth are tracked using a dislocation extraction algorithm (DXA) [51]. The HCP lattices and the void are represented by red atoms and the green area in Fig. 9, respectively. Most of the lattice structure changes are observed near the local voids. In addition, we observe that the void tends to grow toward the atoms experiencing the stacking fault. When a stacking fault occurs at an aluminum atom, the atom excites the neighboring atoms, which promotes dislocation [52]. Consequently, the movement of the excited atoms causes another stacking fault. This chain reaction eventually forms a slip band, as is shown in Fig. 9. While the normal aluminum atoms are arranged regularly, the atoms in the slip band are arranged diagonally. This atomic reordering generates a void. Reordered atoms in a slip band are in a higher energy state than normal atoms. Thus, as the energy state increases due to stretching, unstable atoms in a slip band are more likely to experience bond breakage with neighbors and form a void. As the process is repeated, the small voids present in the matrix coalesce, and the void grows.

Around a strain of 0.2, the second large decrease occurs in the stress–strain curves due to the CNT fracture. Details of the CNT fracture process are captured in Fig. 10. First, the two C–C bonds parallel to the applied loading begin to break near the void in the aluminum matrix. Next, the bond breakage spreads, and the hole expands on the surface. The fracture then propagates perpendicular to the loading direction, eventually leading to a complete break of the CNT.

In Fig. 6, the most dramatic change with increase in CNT diameter is composite toughness. Particularly, the area under the curve between the 0.1 and 0.2 strain values largely increases according to CNT size,

Table 2

Mechanical properties of CNT–Al composites with different CNT sizes.

	Young's modulus (GPa)	Yield stress (GPa)	Yield strain	Fracture stress (GPa)	Fracture strain
(4,4)CNT–Al	97.01	6.48	0.07360	5.02	0.18025
(6,6)CNT–Al	99.02	7.72	0.08290	5.91	0.19085
(8,8)CNT–Al	103.3	8.58	0.08685	8.65	0.18995

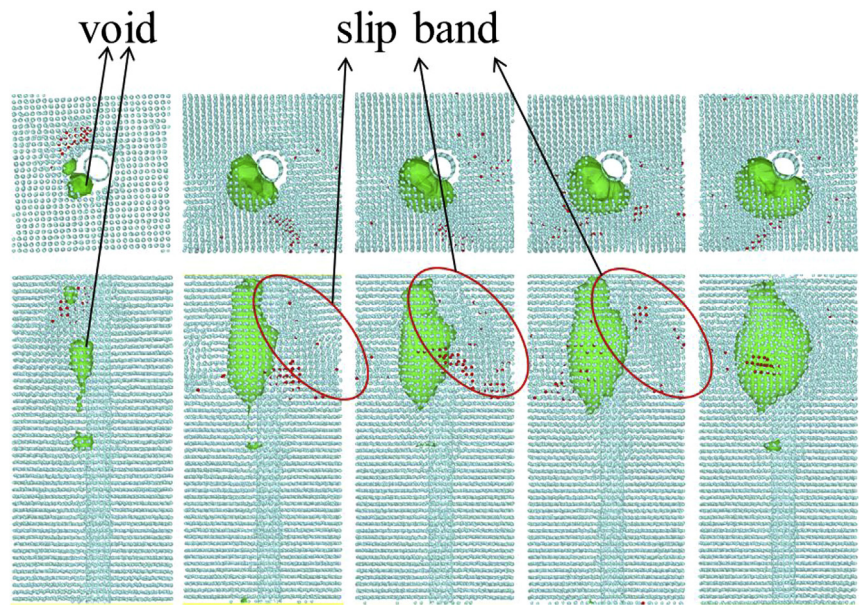


Fig. 9. Snapshots of the MD simulation around 0.1 strain, where the stress–strain curve shows a large decrease. The snapshots show the detailed mechanisms of fracture evolution inside the aluminum matrix. The green denotes a void, and the red represents the HCP lattice structure (For interpretation of the references to color in this figure legend, the reader is referred to the web version of this article.).

which demonstrates that the endurance capability of the composite over external loading is greatly enhanced due to the CNT, even after the aluminum matrix fractures. The toughness of each curve in Fig. 6 and each component shown in Fig. 7 is calculated by integrating the areas under the curve, and the calculations are summarized in Table 3.

Compared to the toughness of pure aluminum, toughness increases of 37% for (4,4)CNT–Al, 72% for (6,6)CNT–Al, and 100% for (8,8)CNT–Al were observed. The 2%, 3%, and 4% volume fraction of CNT contributes to the total energy absorption of approximately 30%, 40%, and 50%, respectively. The calculations reveal that only a small percentage of CNT reinforcement contributes to a dramatic increase in load support.

4. Conclusions

In the present study, MD simulations were conducted in order to investigate the mechanical behavior of CNT-reinforced aluminum composite with various CNT diameters. The stress–strain curves were obtained under tensile loading, and the variations of the curves were analyzed through MD snapshots that enable detailed analyses of atomic behaviors. The overall mechanical properties, such as Young’s modulus and toughness, increased considerably as the CNT reinforcement was increased. Furthermore, component analysis revealed that even a small fraction of CNT can play a significant role in enhancing the mechanical properties of composites. Although excessive external loading can fracture the metal matrix and initiate a crack inside the metal matrix, CNTs withstand additional loading and thereby suspend the entire fracture of the composite by increasing the fracture strain almost two-fold. In addition, the MD simulations offered a detailed fracture mechanism of the MMCs at the atomic scale. For example, the stress decreases were shown to be due to the combination of lattice structure change, dislocation, stacking faults, and micro-void nucleation, whereas these phenomena are rarely observed in real-world experiments.

Table 3
Toughness of CNT reinforcement, aluminum matrix, and CNT–Al composite.

	CNT reinforcement	Al matrix	CNT–Al composite
(4,4)CNT–Al	0.32 GPa (29.2%)	0.78 GPa (70.8%)	1.11 GPa (100%)
(6,6)CNT–Al	0.57 GPa (40.7%)	0.83 GPa (59.3%)	1.39 GPa (100%)
(8,8)CNT–Al	0.76 GPa (46.7%)	0.76 GPa (53.4%)	1.63 GPa (100%)
Pure Al			0.81 GPa

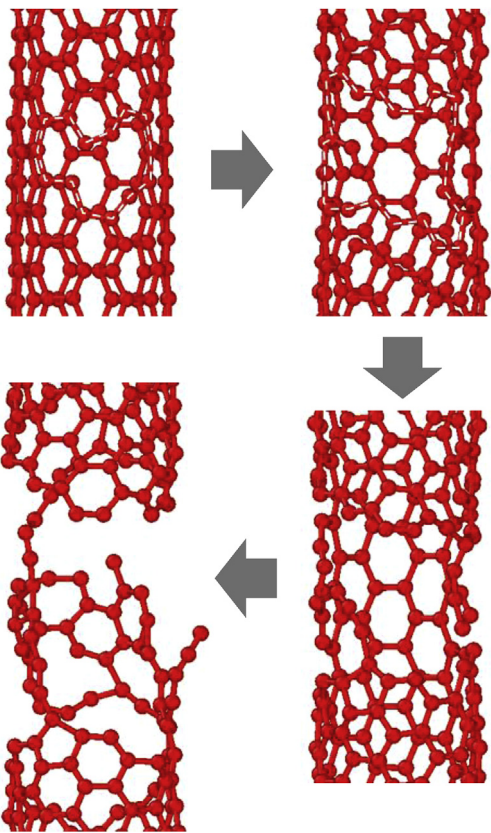


Fig. 10. Representative snapshots of the CNT fracture process.

This study provides a theoretical framework for predicting the mechanical behaviors of MMCs at the atomic scale. The model in this study can be used to investigate the effects of CNT defects, CNT surface coatings, CNT orientations, and different types of CNTs and matrices on the mechanical properties of MMCs. It is of considerable significance that these studies at the atomic scale will reveal the fundamental factors that define the macroscale properties. A multiscale model will be developed to characterize the mechanical properties of MMCs by combining the MD model and a continuum model. It will be a model that can be used to design bulk MMCs with desirable mechanical properties by tailoring the nanoscale variables.

Acknowledgement

This research was supported by the National Research Foundation of Korea (NRF), funded by the Korean government (MEST) (NRF-2015R1A2A2A11027580) and the Ministry of Education (NRF-2015R1D1A1A01057759).

References

- Iijima S. Helical microtubules of graphite carbon. *Nature* 1991;354(7):56–8.
- Che Y, Chen H, Gui H, Liu J, Liu B, Zhou C. Review of carbon nanotube nanoelectronics and macroelectronics. *Semicond Sci Technol* 2014;29(7):073001.
- Dekker C. Carbon nanotubes as molecular quantum wires. *Phys Today* 1999;52:22–30.
- de Heer WA, Châtelain A, Ugarte D. A carbon nanotube field-emission electron source. *Science* 1995;270(5239):1179–80.
- Choi WB, Chung DS, Kang JH, Kim HY, Jin YW, Han IT, et al. Fully sealed, high-brightness carbon-nanotube field-emission display. *Appl Phys Lett* 1999;75(20):3129.
- Chen W, Tu J, Wang L, Gan H, Xu Z, Zhang X. Tribological application of carbon nanotubes in a metal-based composite coating and composites. *Carbon* 2003;41(2):215–22.
- Silvestre N. State-of-the-art review on carbon nanotube reinforced metal matrix composites. *Int J Compos Mater* 2013;3(6A):28–44.
- Jang Y-T, Moon S-I, Ahn J-H, Lee Y-H, Ju B-K. A simple approach in fabricating chemical sensor using laterally grown multi-walled carbon nanotubes. *Sens Actuators B Chem* 2004;99(1):118–22.
- Deo RP, Wang J, Block I, Mulchandani A, Joshi KA, Trojanowicz M, et al. Determination of organophosphate pesticides at a carbon nanotube/organophosphorus hydrolase electrochemical biosensor. *Anal Chim Acta* 2005;530(2):185–9.
- Wang J, Liu G, Jan MR. Ultrasensitive electrical biosensing of proteins and DNA: carbon-nanotube derived amplification of the recognition and transduction events. *J Am Chem Soc* 2004;126:3010–1.
- Salvetat J-P, Bonard J-M, Thomson N, Kulik A, Forro L, Benoit W, et al. Mechanical properties of carbon nanotubes. *Appl Phys A* 1999;69(3):255–60.
- Ruoff RS, Lorents DC. Mechanical and thermal properties of carbon nanotubes. *Carbon* 1995;33(7):925–30.
- Zhang J, Ju S, Jiang D, Peng H-X. Reducing dispersity of mechanical properties of carbon fiber/epoxy composites by introducing multi-walled carbon nanotubes. *Compos Part B Eng* 2013;54:371–6.
- Coleman JN, Khan U, Gun'ko YK. Mechanical reinforcement of polymers using carbon nanotubes. *Adv Mater* 2006;18(6):689–706.
- Wu T-M, Lin Y-W, Liao C-S. Preparation and characterization of polyaniline/multi-walled carbon nanotube composites. *Carbon* 2005;43(4):734–40.
- Kulkarni M, Carnahan D, Kulkarni K, Qian D, Abot JL. Elastic response of a carbon nanotube fiber reinforced polymeric composite: a numerical and experimental study. *Compos Part B Eng* 2010;41(5):414–21.
- Tai N-H, Yeh M-K, Peng T-H. Experimental study and theoretical analysis on the mechanical properties of SWNTs/phenolic composites. *Compos Part B Eng* 2008;39(6):926–32.
- Neubauer E, Kitzmantel M, Hulman M, Angerer P. Potential and challenges of metal-matrix-composites reinforced with carbon nanofibers and carbon nanotubes. *Compos Sci Technol* 2010;70(16):2228–36.
- Bakshi S, Lahiri D, Agarwal A. Carbon nanotube reinforced metal matrix composites – a review. *Int Mater Rev* 2010;55(1):41–64.
- Dorri Moghadam A, Omrani E, Menezes PL, Rohatgi PK. Mechanical and tribological properties of self-lubricating metal matrix nanocomposites reinforced by carbon nanotubes (CNTs) and graphene – a review. *Compos Part B Eng* 2015;77:402–20.
- Perez-Bustamante R, Estrada-Guel I, Antunez-Flores W, Miki-Yoshida M, Ferreira P, Martínez-Sánchez R. Novel Al-matrix nanocomposites reinforced with multi-walled carbon nanotubes. *J Alloys Compd* 2008;450(1):323–6.
- George R, Kashyap K, Rahul R, Yamdagni S. Strengthening in carbon nanotube/aluminium (CNT/Al) composites. *Scr Mater* 2005;53(10):1159–63.
- Esawi A, Morsi K, Sayed A, Taher M, Lanka S. Effect of carbon nanotube (CNT) content on the mechanical properties of CNT-reinforced aluminium composites. *Compos Sci Technol* 2010;70(16):2237–41.
- Tokunaga T, Kaneko K, Horita Z. Production of aluminium-matrix carbon nanotube composite using high pressure torsion. *Mater Sci Eng A* 2008;490(1–2):300–4.
- Bakshi SR, Singh V, Balani K, McCartney DG, Seal S, Agarwal A. Carbon nanotube reinforced aluminium composite coating via cold spraying. *Surf Coat Technol* 2008;202(21):5162–9.
- Kwon H, Leparoux M. Hot extruded carbon nanotube reinforced aluminium matrix composite materials. *Nanotechnology* 2012;23(41):415701.
- He CN, Zhao NQ, Shi CS, Song SZ. Mechanical properties and microstructures of carbon nanotube-reinforced Al matrix composite fabricated by in situ chemical vapor deposition. *J Alloys Compd* 2009;487(1–2):258–62.
- Deng CF, Wang DZ, Zhang XX, Li AB. Processing and properties of carbon nanotubes reinforced aluminium composites. *Mater Sci Eng A* 2007;444(1–2):138–45.
- Esawi AMK, Morsi K, Sayed A, Taher M, Lanka S. The influence of carbon nanotube (CNT) morphology and diameter on the processing and properties of CNT-reinforced aluminium composites. *Compos Part A Appl Sci Manuf* 2011;42(3):234–43.
- Song H-Y, Zha X-W. Influence of nickel coating on the interfacial bonding characteristics of carbon nanotube–aluminum composites. *Comput Mater Sci* 2010;49(4):899–903.
- Xiao S, Hou W. Fracture of vacancy-defected carbon nanotubes and their embedded nanocomposites. *Phys Rev B* 2006;73(11):115406.
- Silvestre N, Faria B, Canongia Lopes JN. Compressive behavior of CNT-reinforced aluminum composites using molecular dynamics. *Compos Sci Technol* 2014;90:16–24.
- Winey JM, Kubota A, Gupta YM. Thermodynamic approach to determine accurate potentials for molecular dynamics simulations: thermoelastic response of aluminum. *Modell Simul Mater Sci Eng* 2010;18(2):029801.
- Stuart SJ, Tutein AB, Harrison JA. A reactive potential for hydrocarbons with intermolecular interactions. *J Chem Phys* 2000;112(14):6472.
- Deb Nath SK, Kim S-G. Study of the nanomechanics of CNTs under tension by molecular dynamics simulation using different potentials. *ISRN Condens Matter Phys* 2014;2014:18.
- Wei Y, Wu J, Yin H, Shi X, Yang R, Dresselhaus M. The nature of strength enhancement and weakening by pentagon–heptagon defects in graphene. *Nat Mater* 2012;11(9):759–63.
- Munilla J, Castro M, Carnicero A. Surface effects in atomistic mechanical simulations of Al nanocrystals. *Phys Rev B* 2009;80(2).
- Komanduria R, Chandrasekaran N, Raff LM. Molecular dynamics (MD) simulation of uniaxial tension of some single-crystal cubic metals at nanolevel. *Int J Mech Sci* 2001;43:2237.
- Wen Y-H, Zhu Z-Z, Zhu R-Z. Molecular dynamics study of the mechanical behavior of nickel nanowire: strain rate effects. *Comput Mater Sci* 2008;41(4):553–60.
- Wen Y-H, Zhu Z-Z, Shao G-F, Zhu R-Z. The uniaxial tensile deformation of Ni nanowire: atomic-scale computer simulations. *Phys E* 2005;27(1–2):113–20.
- Setoodeh AR, Attariani H, Khosrownejad M. Nickel nanowires under uniaxial loads: a molecular dynamics simulation study. *Comput Mater Sci* 2008;44(2):378–84.
- Koh SJ, Lee HP. Molecular dynamics simulation of size and strain rate dependent mechanical response of fcc metallic nanowires. *Nanotechnology* 2006;17(14):3451–67.
- Subramaniyan AK, Sun CT. Continuum interpretation of virial stress in molecular simulations. *Int J Solids Struct* 2008;45(14–15):4340–6.
- Sankaranarayanan S, Bhethanabotla V, Joseph B. Molecular dynamics simulation of temperature and strain rate effects on the elastic properties of bimetallic Pd–Pt nanowires. *Phys Rev B* 2007;76(13).
- Lee S, Park J, Yang J, Lu W. Molecular dynamics simulations of the traction-separation response at the interface between PVDF binder and graphite in the electrode of Li-ion batteries. *J Electrochem Soc* 2014;161(9):A1218–23.
- Ru CQ. Effective bending stiffness of carbon nanotubes. *Phys Rev B* 2000;62(15):9973–6.
- Laha T, Chen Y, Lahiri D, Agarwal A. Tensile properties of carbon nanotube reinforced aluminum nanocomposite fabricated by plasma spray forming. *Compos Part A Appl Sci Manuf* 2009;40(5):589–94.
- Choi HJ, Shin JH, Bae DH. The effect of milling conditions on microstructures and mechanical properties of Al/MWCNT composites. *Compos Part A Appl Sci Manuf* 2012;43(7):1061–72.
- Yang Z, Lu Z, Zhao Y-P. Atomistic simulation on size-dependent yield strength and defects evolution of metal nanowires. *Comput Mater Sci* 2009;46(1):142–50.
- Honeycutt JD, Andemen HC. Molecular dynamics study of melting and freezing of small Lennard-Jones clusters. *J Phys Chem* 1987;91:4950–63.
- Stukowski A. Computational analysis methods in atomistic modeling of crystals. *J Miner Met Mater Soc* 2013;66(3):399–407.
- Sorensen MR, Brandbyge M, Jacobsen KW. Mechanical deformation of atomic-scale metallic contacts: structure and mechanisms. *Phys Rev B* 1998;57(6):3283–94.